



HAL
open science

Opal Synthesis: Toward Geologically Relevant Conditions

Simon Gouzy, Benjamin Rondeau, Vassilissa Vinogradoff, Boris Chauviré,
Marie-Vanessa Coulet, Olivier Grauby, Hélène Terrisse, John Carter

► **To cite this version:**

Simon Gouzy, Benjamin Rondeau, Vassilissa Vinogradoff, Boris Chauviré, Marie-Vanessa Coulet, et al.. Opal Synthesis: Toward Geologically Relevant Conditions. Minerals, 2024, 14, 10.3390/min14100969 . hal-04768021

HAL Id: hal-04768021

<https://hal.science/hal-04768021v1>

Submitted on 5 Nov 2024

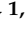



HAL is a multi-disciplinary open access archive for the deposit and dissemination of scientific research documents, whether they are published or not. The documents may come from teaching and research institutions in France or abroad, or from public or private research centers.

L'archive ouverte pluridisciplinaire **HAL**, est destinée au dépôt et à la diffusion de documents scientifiques de niveau recherche, publiés ou non, émanant des établissements d'enseignement et de recherche français ou étrangers, des laboratoires publics ou privés.



Distributed under a Creative Commons Attribution 4.0 International License

Opal Synthesis: Toward Geologically Relevant Conditions

Simon Gouzy ^{1,2,*}, Benjamin Rondeau ¹ , Vassilissa Vinogradoff ², Boris Chauviré ³ , Marie-Vanessa Coulet ⁴ , Olivier Grauby ⁵, Hélène Terrisse ⁶  and John Carter ^{7,8}

- ¹ Nantes Université, Univ Angers, Le Mans Université, CNRS, Laboratoire de Planétologie et Géosciences, LPG UMR 6112, 44000 Nantes, France; benjamin.rondeau@univ-nantes.fr
- ² Aix-Marseille Université, CNRS UMR 7345, Physique des Interactions Ioniques et Moléculaires (PIIM), 13013 Marseille, France; vassilissa.vinogradoff@univ-amu.fr
- ³ GeoGems, 44350 Guérande, France; boris.chauvire@gmail.com
- ⁴ Aix-Marseille Université, CNRS UMR 7246, MADIREL, 13013 Marseille, France; vanessa.coulet@univ-amu.fr
- ⁵ Aix-Marseille Université, CNRS UMR 7325, CINaM, 13009 Marseille, France; olivier.grauby@univ-amu.fr
- ⁶ Nantes Université, CNRS, Institut des Matériaux de Nantes Jean Rouxel, IMN, 44000 Nantes, France; helene.terrisse@cnrs-imn.fr
- ⁷ Institut d'Astrophysique Spatiale, CNRS, Université Paris-Saclay, 91405 Orsay, France; john.carter@ias.u-psud.fr or john.carter@lam.fr
- ⁸ Aix-Marseille Université, CNES, CNRS UMR 7326, LAM, 13388 Marseille, France
- * Correspondence: simon.gouzy@univ-nantes.fr or simon.gouzy@gmail.com

Abstract: Natural opal is a widespread mineral formed by the aqueous alteration of silicate rocks. It occurs as a mixture of silica nano-to-micro-structures (e.g., nanograins, spheres) and silica hydrogel cement, with variations in the proportions of these components leading to significant differences in the physico-chemical properties of opals. However, the detailed process of their formation in nature and the influence of the mixing ratio are not fully understood, as opal has not been yet synthesized under geologically relevant conditions. This study aims to develop a method of opal synthesis in conditions close to continental weathering conditions (<50 °C, ambient pressure) using relevant chemicals that could be employed to gain insight into the processes that give rise to opal on Earth and Mars. Our synthesis method enabled us to synthesize opal-A with different mixing ratios, of which four were then studied to determine the effect on the material's properties. Changes in the proportion of the hydrogel cement affect the porosity and the total water content, as well as the proportion of "water" species (H₂O and OH). Moreover, the synthetic opal obtained with a 1:1 ratio shows the closest similarity to natural opal-AG. Finally, our results support the hypothesized multistage process for opal formation in nature.

Keywords: opal; natural opal; synthetic opal; synthesis; earth; mars; amorphous silica; structure; opaline silica; analogue



Citation: Gouzy, S.; Rondeau, B.; Vinogradoff, V.; Chauviré, B.; Coulet, M.-V.; Grauby, O.; Terrisse, H.; Carter, J. Opal Synthesis: Toward Geologically Relevant Conditions. *Minerals* **2024**, *14*, 969. <https://doi.org/10.3390/min14100969>

Academic Editor: Olev Vinn

Received: 15 August 2024

Revised: 23 September 2024

Accepted: 24 September 2024

Published: 26 September 2024



Copyright: © 2024 by the authors. Licensee MDPI, Basel, Switzerland. This article is an open access article distributed under the terms and conditions of the Creative Commons Attribution (CC BY) license (<https://creativecommons.org/licenses/by/4.0/>).

1. Introduction

Natural opal (amorphous hydrated silica, or opaline silica, SiO₂·nH₂O) is an amorphous-to-poorly-crystallized species of silica containing up to 18 wt% of cumulated molecular water and bound hydroxyls (Si-OH, silanols) [1–5]. On the basis of X-ray diffraction, the structural classification of opal defines three main types: opal-A, which is amorphous to highly disordered; opal-CT, amorphous with α-cristobalite crystallites with α-tridymite stacking defects; and opal-C, amorphous with well-ordered α-cristobalite [2,6–10]. These opal types also provide specific NMR, Raman, and infrared signatures [3,11–17]. Opal-C proved to be a variety of opal-CT without any tridymitic defect stacking [7]. As a consequence, in this manuscript, we use the term "opal-CT", in order to include opal-C. Additionally, opal-A has been subdivided into opal-AG (G for gel) and opal-AN (N for network) on the basis of small-angle X-ray diffraction and neutron scattering [3].

At a larger scale, and independently of the atomic structure, natural opals are composed of silica nanograins about 25 nm in diameter cemented by an amorphous silica hydrogel (to the exception of opal-AN) [8].

Depending on the deposit, the formation processes, and the type of opal (A or CT), the nanograins can arrange into a large variety of structures. Opal-A nanograins assemble in concentric agglomerates called ‘spheres’, while opal-CT nanograins assemble in one-dimensional ‘fibers’, two-dimensional ‘platelets’, stacked platelets, called ‘tablets’, and interlocking platelets in spherical aggregates, called ‘lepispheres’ [8].

A gemological distinction is also made between opal that shows play-of-color, with pure spectral colors moving on the surface of the stone as it is tilted (also referred to as precious opal), and common opal, which does not display such play-of-color [18].

Besides the biomineralization of opal by living organisms for their skeleton, opal forms through the aqueous alteration of silicate rocks. This occurs through either continental weathering [19–27] or hydrothermal alteration [28–35], in various geological contexts (e.g., acidic volcanic traps, alluvial fans and deltas, hydrothermal hot springs). Terrestrial observations, coupled with water–rock alteration experiments, show that opal forms at various scales (large outcrops of up to several km), at the expense of various minerals (e.g., feldspars, volcanic glass, clays, and olivine) [14,23,24,26,36]. Opal forms surface deposits such as silica sinters, or occurs as underground cavity or porosity filler [14,26,36–41]. For all these abiotic processes, the formation process of opal in nature is supposed to follow several continuous steps that may overlap and depend on multiple physico-chemical parameters (temperature, pH, ionic strength, and silica concentration) (Figure 1), as follows:

1. Monomeric silica in groundwater polymerizes and progressively forms polysilicic acids. These silica polymers internally condense into nanometer-sized silica colloids named “nanograins” (nucleation process) [42–44].
2. The colloids grow and merge by Ostwald ripening and by the addition of low polymeric silica in their outer layer [42–44].
3. Depending on the fluid’s chemical composition and evolution, physical parameters (e.g., viscosity), and changes in dynamics (e.g., flow rate), the silica nanograins eventually arrange into an aggregated structure [45–47], hereafter called “spheres”.
4. Deposition by gravity and the arrangement of the nanograins and the eventual spheres at the bottom of the cavity. This optionally may lead to a diffracting array responsible for play-of-color [8,48].
5. The pores between the deposited silica nanograins and/or the spheres are partially or entirely filled by amorphous silica hydrogel [42], thus closing the fluid percolating system.

However, this scenario for opal formation has not been extensively tested yet in the laboratory. Several attempts to synthesize opal have been conducted, and the resulting products share some similarities with natural opal, but none of the synthesis methods have used geologically relevant compounds or conditions. The most commonly used method, established by Stöber in the late 1960s [49], is based on the hydrolysis of tetraethoxysilane (TEOS) in organic solvent with ammonia. Recent adaptations of this method mainly used organic compounds as the main solvent [50–55], or more exotic routines involving high-temperature or high-pressure conditions [56–58]. The synthesis of silica spheres with diameters ranging from 150 to 300 nanometers opened the way for the synthesis of colloidal photonic crystals mimicking the visual play-of-color of natural opal. The synthesis of silica nanograins and spheres is now widely studied, and several methods have been developed for applications in various domains, such as chemistry (e.g., catalyst bases), textile and papers (e.g., pigments and latex–foam products), medicine (e.g., drug delivery), etc. [42,59–61]. However, the syntheses developed in these studies are unrealistic for geological contexts and conditions. For example, the spheres are grown in organic compounds (ethanol or others) as the main solvents, whereas the main solvent on the Earth’s surface remains water.

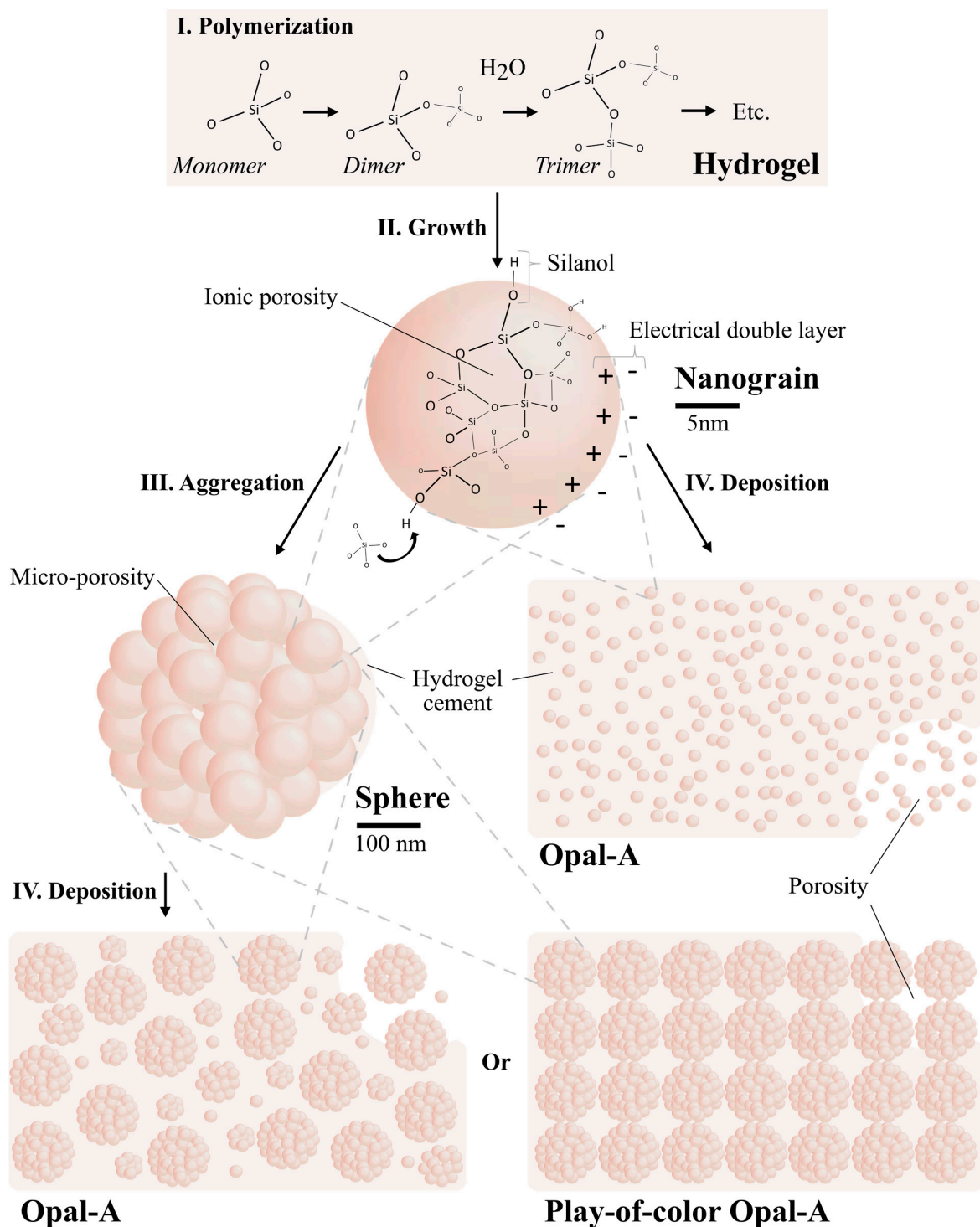


Figure 1. Schematic diagram showing the progressive organization of silica-forming natural opal-A.

Another series of studies attempted to produce silica particles under much more geologically relevant conditions, using only silica dissolved in pure water [43,44,62–65]. In some studies, this was motivated by the understanding of formation of silica scale in geothermal industry [66–68]. Although these experimental studies successfully produced silica particles, they did not produce solids, mostly because of very low yields, due to the low silica solubility in the investigated pH range.

For these reasons, we developed a method to produce synthetic opals starting from a solution and ending with a cohesive solid product, with properties as close as possible

to the natural ones, using compounds and processes compatible with natural conditions: we stirred the solutions in order to model the fluid flow that naturally occurs; we used water as the solvent; the temperature was restricted to the 20–50 °C range, coinciding with known weathering temperatures; and drying in an oven at 80 °C was performed to remove the excess of water in order to model the drying of natural silica. Preliminary experiments with drying at 50 °C provided samples with exactly the same properties, but this required a much longer experimental time. In order to save time, we performed drying at 80 °C, although this temperature is too high for continental weathering conditions. Additionally, we conceded an anomalously high pH in order to increase silica solubility and, hence, increase the synthesis yield.

First, we investigated the formation and growth of silica nanograins in an aqueous potassium hydroxide solution and the aggregation of these nanograins into larger structures. We chose potassium hydroxide for this first attempt at chemical modeling of a natural system, because potassium is a common impurity in natural opal, and potassium plays a role in the growth of the silica nanograins [42]. To obtain a microstructure resembling that of natural opal, we incorporated silica hydrogel in various proportions (varying silica nanograins/hydrogel volume ratios). Second, we investigated the effect of this volume ratio (silica nanograins/hydrogel) on the material properties.

Due to the diversity and complexity of the formation environments and the opals themselves [8,69], it is particularly challenging to assess the impact of each formation condition (e.g., pH, temperature) and the chemical composition of the fluids on both opal chemistry and properties (e.g., atomic structure, silica structure). Therefore, in order to better understand opals, it is necessary to find alternatives, such as synthesis, in conditions approaching geologically relevant conditions on Earth. The intended application of this work extends beyond the terrestrial context, as we also seek to better understand the local aqueous environments leading to opal precipitation on ancient Mars. Opal is a common alteration product that has been found throughout Mars in terrains spanning geological eons, and that has been proposed to belong to a subset of known terrestrial settings [70,71].

2. Experimental Method

2.1. Materials

Sodium metasilicate (Na_2SiO_3 ; CAS# 6834-92-0, 50 to 53% of SiO_2), potassium hydroxide (KOH; CAS# 1310-58-3, $\geq 90\%$ purity), and the cation exchange resin (Amberlite IRC120 H form, CAS# 39389-20-3) used for the synthesis of opal were purchased from Sigma-Aldrich (Burlington, Massachusetts, United States). Ultrapure water (0.055 $\mu\text{S}/\text{cm}$ conductivity and 18.2 M Ω resistivity at 25 °C) was produced at the Laboratoire de Planétologie et Géosciences (Nantes, France) with a Merck Millipore Milli Q Integral 10 and used as the only solvent. All materials were used as received.

2.2. Experimental Procedure

In order to simulate the natural release of silica in solution, we used an ion-exchange method with sodium metasilicate [72]. This technique substitutes sodium atoms with hydrogen on the exchange sites. It allows the release of monomeric silica (soluble silica) without adding any other chemical compound not found in nature that could induce undesired *in situ* reactions.

The synthesis method involves three main steps designed to mimic the hypothesized natural opal growth steps: (1) synthesis of silica nanograins; (2) synthesis of silica hydrogel; (3) combination of nanograins and hydrogel. The temperature was maintained in a range between 20 °C and 50 °C.

2.2.1. Preparation of Silica Nanograins

A total of 14 g of sodium metasilicate (Na_2SiO_3) powder was dissolved in 100 mL of ultrapure water (1.147 mol/L) by stirring using a magnetic bar at 300 rpm; the solution was passed through a 300 mL column filled with cation exchange resin (Figure 2, part 1).

We assumed that every mole of Na_2SiO_3 was exchanged into $\text{Si}(\text{OH})_4$. The resulting silicic acid solution (1.456 mol/L of $\text{Si}(\text{OH})_4$ at pH = 3) was then added, at a speed of 2 mL per minute using a peristaltic pump, into a beaker containing 0.5 g of potassium hydroxide dissolved in 20 mL of ultrapure water (1.147 mol/L) (0.445 mol/L; pH > 13.5) (Figure 2, part 2). In accordance with the diffusion-limited growth equations in [73], a slow release of silica monomer was chosen to limit nucleation and thus promote the growth of colloids. Potassium acts as a natural pH buffer and as an extra electrolyte in the solution, which compresses the thickness of the electrical double layer on colloidal silica surfaces [72,74]. Thus, it tends to inhibit aggregation of silica nanograins and favor their individual and progressive growth. Although the alkaline pH is likely to change a proportion of the silica monomers into deprotonated species such as $\text{SiO}(\text{OH})_3^-$ and $\text{SiO}_2(\text{OH})_2^{2-}$ and generate dimers, trimers, and tetramers [75], we did not investigate the effect of such changes on the obtained synthetic product. During the incorporation, the receiving beaker was stirred with an orbital shaker set to 100 rpm and heated at 50 °C. Next, the solution was placed at room temperature (21 °C) for 40 h under stirring with an orbital shaker set to 100 rpm, to attempt to increase the size of the silica colloids (growth step) to a dimension close to that of natural nanograins in opals (up to 25 nm) (Figure 2, part 3).

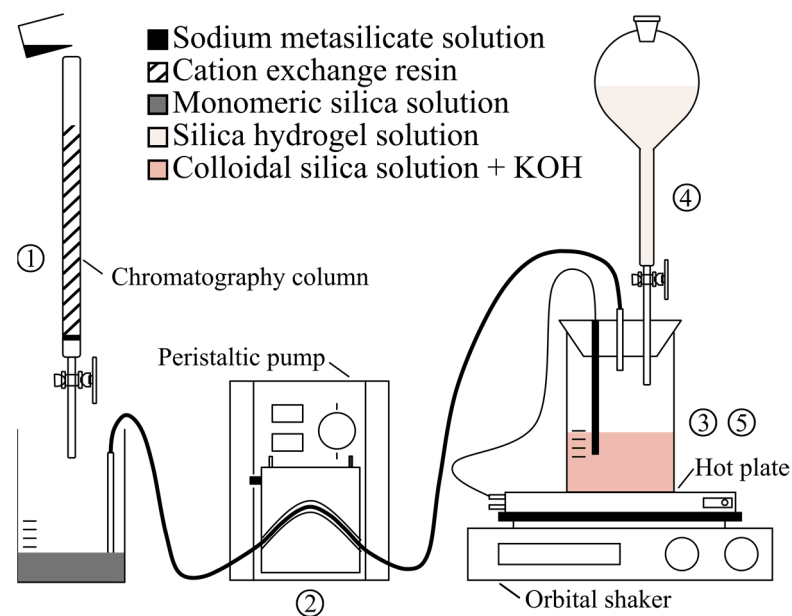


Figure 2. Experimental apparatus for the synthesis routine used in this study. Numbers in circles refer to synthesis steps detailed in the text.

2.2.2. Preparation of Silica Hydrogel

A total of 14 g of sodium metasilicate (Na_2SiO_3) was dissolved in 100 mL of ultrapure water and passed through a 300 mL column filled with cation exchange resin. The resulting silicic acid solution (1.456 mol/L of $\text{Si}(\text{OH})_4$; pH = 3) was then stored for 2 to 3 h at room temperature (Figure 2, part 4).

2.2.3. Opal Synthesis

The silica hydrogel solution (pH = 3) was added to the silica nanograin solution (pH = 10.5) and stirred with a continuously decreasing speed from 100 to 0 rpm for 5 h (Figure 2, part 5) at room temperature. The obtained solution (pH = 8.5) was stored for 3 days (72h) to allow time for the aggregates to settle at the bottom of the beaker and for the hydrogel to harden. Due to the change in pH, the potassium no longer acted as an extra electrolyte, but as a flocculating agent (bridging ion) [42]. Finally, the solution was placed in an oven at 80 °C to evaporate the excess water. The heating was stopped when a compact, solid material was formed and no liquid solution remained (approximately 10 days).

This experimental procedure corresponds to a volume ratio of 1:1 between colloidal silica and hydrogel solutions. This synthesis is named Op1:1 hereafter. In order to study different proportions and interactions between hydrogel and nanograins, we varied this ratio by adding more or less hydrogel solution. Four mixtures of nanograins and hydrogel were prepared (Op1:0, Op1:0.5, Op1:1 and Op1:2), from no hydrogel (Op1:0) to hydrogel constituting two-thirds of the product volume (Op1:2) (Table 1).

Table 1. List of syntheses and adopted parameters.

Sample	Nanograin Solution				Hydrogel Solution	
	Na ₂ SiO ₃		KOH		Na ₂ SiO ₃	
	C (mol/L)	V (mL)	C (mol/L)	V (mL)	C (mol/L)	V (mL)
Op1:0	1.147	100	0.445	20	/	/
Op1:0.5	1.147	100	0.445	20	1.147	50
Op1:1	1.147	100	0.445	20	1.147	100
Op1:2	1.147	100	0.445	20	1.147	200

2.3. Methods

2.3.1. Dynamic Light Scattering (DLS)

The hydrodynamic diameter of nanograins was determined by Dynamic Light Scattering (DLS) using a Malvern Zetasizer NanoZS at the Institut des Matériaux Jean Rouxel (Nantes Université, Nantes, France). The measurements were performed in a 1 mL polystyrene cell using a 633 nm He-Ne laser source, with a scattering angle of 173° calibrated on the main refractive index of silica (1.458) and on the viscosity of water at 25 °C. The data were acquired during the growth step of the preparation of silica nanograins. Measurements were taken over 70 s and reproduced 3 times on each sample with manual stirring between each measurement. Indeed, according to the Stokes equation for the flow of a Newtonian incompressible fluid in steady state and at low Reynolds number, a silica particle with small size has a fast falling speed (5.39×10^{-3} cm/s for a silica particle 30 nm in diameter based on Stokes equations). It is therefore mandatory to shake the cell before each measurement in order to identify the true population of silica particles. The data were then processed using the same software used for the acquisition.

2.3.2. Scanning Electron Microscopy (SEM)

We acquired secondary electron images of our samples using two distinct Scanning Electron Microscopes (SEM), both operating at 5 kV: a JEOL JSM 7600F at the Institut des Matériaux Jean Rouxel (Nantes Université, Nantes, France) on fresh break surfaces, and a JEOL JSM-7900F at the Centre Interdisciplinaire de Nanosciences de Marseille (CINAM, Marseille, France) (both operating at 10^{-5} mbar) on powdered samples, all coated with platinum. The samples did not require hydrofluoric acid treatment, which is typically necessary for the preparation of natural opal samples in order to reveal the underlying structure hidden by the hydrogel. In turn, the porosity of the samples induced significant charge accumulation effects under the electron beam, which rendered difficult the acquisition of high-magnification images.

2.3.3. Loss on Drying (LOD)

Weight Loss On Drying (LOD) experiments were performed using a Ney Vulcan 3-1450 box furnace at the Laboratoire de Planétologie et Géosciences (Nantes Université, Nantes, France). For each measurement, 1 g of sample was coarsely powdered using an agate mortar and then transferred into an alumina crucible that was put into the furnace at 1050 °C for 1 h. The initial amount of water (wt.%) was estimated by the difference in mass of the samples before and after drying.

2.3.4. Gas Adsorption

Nitrogen adsorption–desorption isotherms were measured at 77 K on a Micromeritics Gemini apparatus at the MADIREL laboratory (Aix-Marseille Université, Marseille, France). For some samples, the isotherms were also measured using a BELSORP Max 1, in the same laboratory. This apparatus allows lower pressure values and thus enables the characterization of microporosity in the samples. Prior to the sorption measurements, the samples were evacuated in a dynamic vacuum at 80 °C for 15 h in order to remove adsorbed species on their surfaces. About 80–100 mg of powdered sample were used for each measurement. The total porous volume was determined for $p/p^\circ = 0.99$ (with p the relative equilibrium pressure of the adsorbable gas, and p° its saturating vapor pressure), as all pores were filled in with adsorbable nitrogen at this value. The available surface area was calculated using the Brunauer–Emmett–Teller (BET) method [76] and the Barrett, Joyner, and Halenda (BJH) method [77] was applied to the desorption branch of the isotherms to estimate the pore size distribution.

2.3.5. Inductively Coupled Plasma Optical Emission Spectroscopy (ICP-OES)

The quantification of major elements was carried out using a Thermo-Fisher iCAP 6300 ICP-OES at the Laboratoire de Planétologie et Géosciences (Nantes Université, Nantes, France). In total, 100 mg of sample were finely powdered using an agate mortar and mixed with 300 mg of lithium metaborate (LiBO_2). The mixed product was placed in a Ney Vulcan 3-1450 box furnace at 1030 °C for 15 min up to the complete fusion of the sample. The glass obtained was then immersed in a 10% nitric acid solution (HNO_3) until complete dissolution. Standard solutions were prepared with the same method. JW-2, GSP2, USGS AGV-2, USGS BIR-1, and USGS BHVO-2 [78] rock standards were used as reference material for calibration, as well as for instrument drift correction in the case of JW-2. All elemental concentrations were calculated relative to the ^{11}B isotope chosen as the standard. Elemental concentrations were calculated using the Reduce internal software of the Laboratoire de Planétologie et Géosciences (Nantes Université, Nantes, France), and instrumental drift was corrected by linear interpolation using the same software.

2.3.6. Raman Spectroscopy

Raman spectroscopy was performed using a Horiba Jobin-Yvon LabRamHRevo spectrometer equipped with an 1800 lines/mm grating and a $\times 50$ Olympus objective, at the Laboratoire de Planétologie et Géosciences (Nantes Université, Nantes, France). The light source was a solid-state unpolarized laser operating at 532 nm with a power of 150 mW. We used a 200 μm hole. The spectrometer was calibrated on a silicium plate between each sample measurement. Spectra were acquired continuously between 100 and 4000 cm^{-1} in 5 segments by LabSpec 6 acquisition software for durations between 20 and 40 s (depending on the quality of the spectrum), with an average of 10 repetitions. Measurements were taken on fresh break surfaces. Raman spectra were then processed using the OriginPro 8 software (OriginLab, Northampton, MA, USA).

3. Results

3.1. Silica Nanograin Dimensions

The average hydrodynamic diameter of the silica nanograins progressively increases with stirring from 8 nm at $t = 0$ h (99.9% volume), through 14 nm at $t = 20$ h (97.1% volume), to 34 nm at $t = 40$ h (88.8% volume). Figure 3 shows DLS plots of the evolution of the nanograins' hydrodynamic diameters in the colloidal solution during the 40 h of stirring at 0 h, 20 h, and 40h (Figure 3). The presence of another population with sizes between 100 and 500 nm progressively increases with the stirring time, from 2.7% volume at 20 h to 11% volume at 40 h. Due to the wide size range (100–500 nm) and their relative increase in proportion with time compared to the silica nanograins, it was deduced that such populations correspond to silica nanograin aggregates, i.e., spheres (see Figure 1) that are formed during the stirring, and not individual particles.

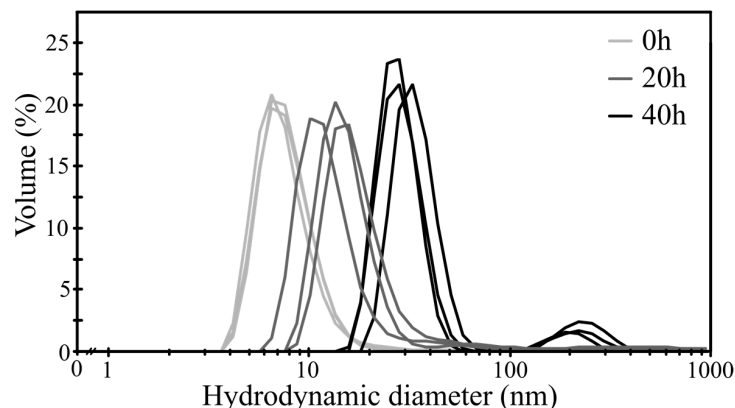


Figure 3. Hydrodynamic diameters of silica colloids at 0, 20, and 40 h of stirring during the growth step (21 °C). The three lines of same color on the graph correspond to three successive measurements of each solution.

3.2. Synthetic Opal Characterization

3.2.1. Visual Aspect

The samples are white and did not show any play-of-color. Figure 4 shows photographs of the top and side of the synthesized sample fragments. When increasing the volume ratio of the hydrogel solution in the synthesis, the samples become more transparent and smoother to the touch. Most of the samples containing hydrogel show an increasing in transparency from the bottom to the top. Op1:1 shows a homogeneous translucent white appearance. Soaked in water, all the samples become colorless and transparent. This phenomenon, observed in some natural opals, is referred to as the “hydrophane” character in the geological and gemological literature [18]. The white color is due to the presence of pores that scatter the visible light. This optical phenomenon is fully reversible by re-drying the solid at room temperature and does not alter the brittleness of the opal. The optical transition from translucent to transparent takes a few seconds for the samples with low hydrogel content (Op1:0.5) or no hydrogel (Op1:0), and about one minute for the samples with higher hydrogel content (Op1:1, Op1:2).

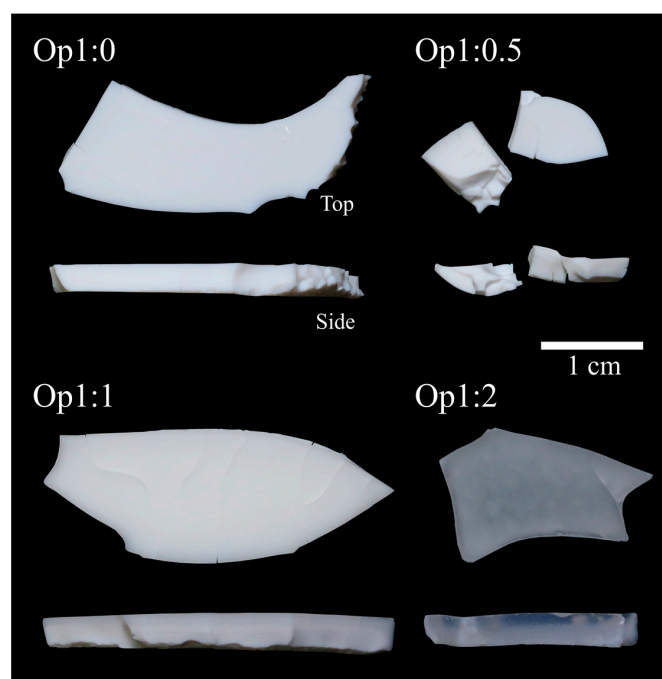


Figure 4. Photographs of the four synthesized samples with, for each, both top and side views.

3.2.2. Microscopic Aspect

Figure 5 shows SEM microphotographs of the fresh break surfaces of the four samples. All the samples show rounded silica nanograins with diameters between 25 and 40 nm (a closer view is given in Figure 6 for Op1:1, as an example), consistent with the DLS measurements. Without the presence of hydrogel cement (Op1:0, Figure 5a), the nanograins are remarkably well visible, and chaotically arranged in more or less compacted regions. In all the samples, the nanograins tend to coalesce into larger aggregates, protospheres (50–300 nm) composed of a few joined nanograins (Figure 6). The incorporation of hydrogel increased the amount of spherical structures in the synthesized products. Hence, the protospheres are no longer simply fused at the nanograin interfaces, but also cemented by the hydrogel (Figure 6). By increasing the volume ratio of the hydrogel solution, the products contain fewer visible large mesopores and the observed surface becomes much smoother and more homogeneous (Figure 5b,c). The hydrogel seems to act as a porosity filler and so a cement of the solid material composed of nanograins, as shown in Figure 6.

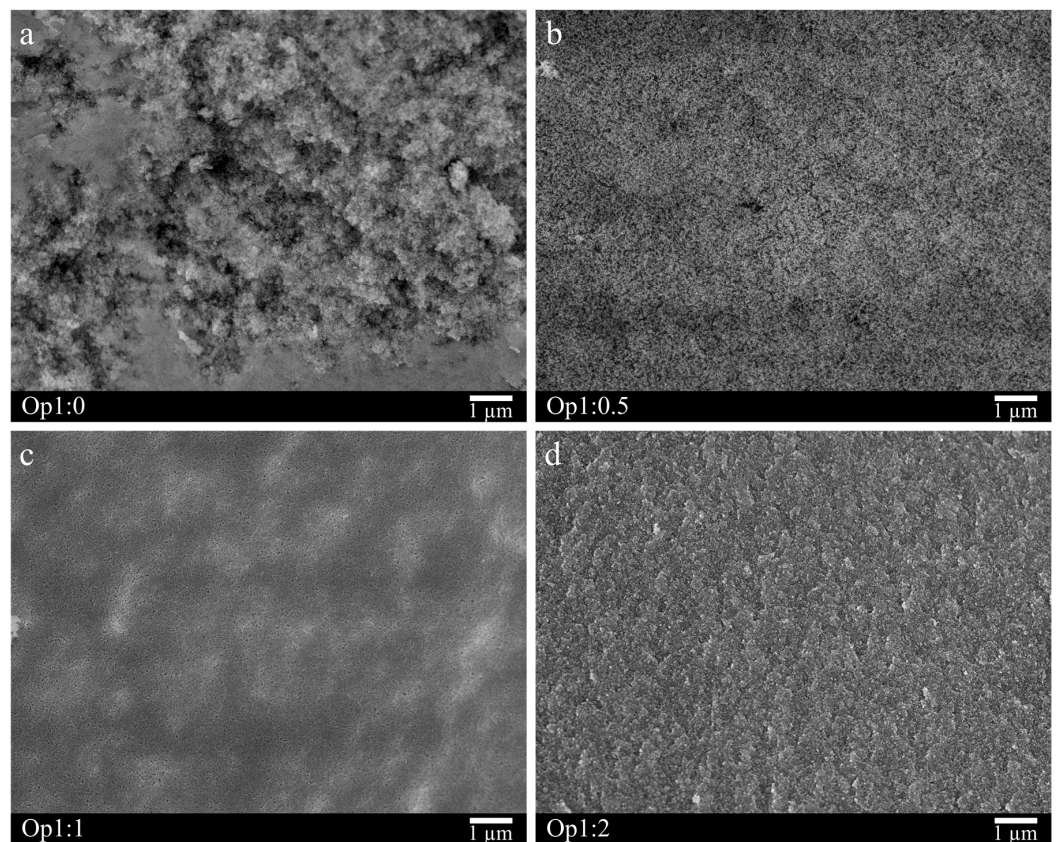


Figure 5. SEM micrographs (10,000 \times , secondary electrons) of fresh break surfaces of synthesized opal: (a) Op1:0, (b) Op1:0.5, (c) Op1:1 and (d) Op1:2. Pores appear in black.

3.2.3. Texture

The adsorption–desorption isotherms are given in Figure 7a. According to the IUPAC classification, they can be assigned to the type-IV isotherms given by the mesoporous samples. Except for Op1:2, the saturation plateau is very short and limited to a few pressure values, which suggests the presence of large mesopores. Increasing the amount of hydrogel in the samples leads to higher specific surface areas (from 21 to 158 m²/g) and porous volumes (from 0.20 to 0.39). The C parameter values, related to surface polarity, are similar for all the samples, suggesting that the surface polarity is not modified by the hydrogel proportion. The specific surface areas are given in Table 2, together with the C parameter. The total porous volume calculated at $p/p^{\circ} = 0.99$ is also given.

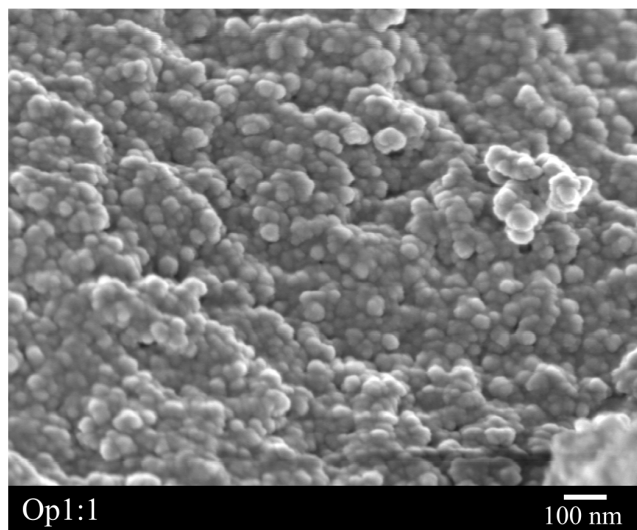


Figure 6. SEM micrograph ($\times 80,000$, secondary electrons) of the powdered sample Op1:1.

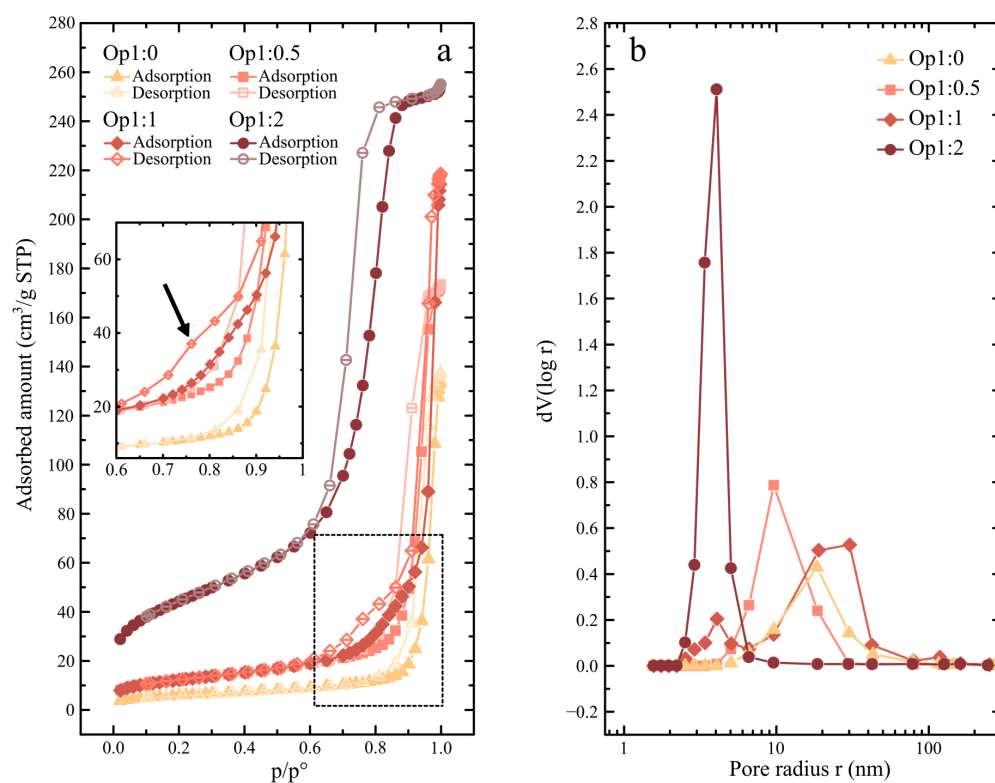


Figure 7. (a) Nitrogen adsorption (full symbols) and desorption (open symbols) isotherms measured at 77 K for the four samples. The black arrow points to a change in the slope of the desorption branch of Op1:1 that can be attributed to the onset of a new pore. (b) Pore radius distribution curves of the four samples.

Table 2. Results obtained by gas adsorption measurements.

Sample	Specific Surface Area (m^2/g)	C Parameter	Porous Volume at $p/p^\circ = 0.99$
Op1:0	21 ± 1	130	0.20
Op1:0.5	44 ± 2	143	0.26
Op1:1	44 ± 2	140	0.32
Op1:2	158 ± 2	145	0.39

The hysteresis between the adsorption and desorption branches becomes larger with increasing the amount of hydrogel in the sample. This is accompanied by the onset in the desorption branch of a shoulder (clearly visible for Op1:1, see arrow in Figure 7a). These features suggest that the pore size decreases and that, especially for Op1:0.5 and Op1:1, a second pore size population is present.

In order to further document the pores in our samples, the pore size distributions were calculated using BJH formalism (Figure 7). The pore size distribution is monomodal for three samples. The pore size decreases from samples Op1:0 to Op1:0.5 to Op1:2. Only sample Op1:1 shows a bimodal distribution, with a minor contribution of pores about 4 nm in size, and a major contribution of pores 10 to 40 nm in size. If this last population of large pores is considered separately, the average pore size decreases from 20 nm to 4 nm as the amount of hydrogel is increased.

3.2.4. Chemical Composition

The chemical composition of the samples was measured by ICP-OES and LOD. All the samples contain a detectable amount of silicon, potassium, and water (Table 3). The amount of water in the samples increases as the volume ratio of the hydrogel increases, from 8.2 ± 0.10 wt% (Op1:0.5) to 12 ± 3.54 wt% (Op1:1) to 34 ± 7.10 wt% (Op1:2), with the notable exception of sample Op1:0 (which does not contain hydrogel), which had 9.0 ± 0.14 wt% of water.

Table 3. ICP-OES (SiO₂ and K₂O) and LOD (H₂O) measurements of the chemical composition of the synthetic opals expressed in weight percentage. Al₂O₃, MgO, CaO, and Na₂O were measured and below detection limits (<0.0098, 0.0023, 0.0122, and 0.0034, respectively).

Sample	SiO ₂	K ₂ O	H ₂ O
Op1:0	85 ± 1.2	6.1 ± 0.1	9.0 ± 0.14
Op1:0.5	86.5 ± 0.8	5.1 ± 0.2	8.2 ± 0.10
Op1:1	83.9 ± 1.0	3.4 ± 0.3	12.0 ± 3.54
Op1:2	62.2 ± 0.7	1.8 ± 0.2	34.0 ± 7.10

3.2.5. Raman Properties

The Raman spectra of all the samples are shown in Figure 8, together with the spectrum of a white opal-AG from Honduras, taken as a natural reference opal (named opal-AG in Figure 8). All the spectra share peaks in common with the natural opal-A at 430, 490, 795, 830, 970, 1065, 1190, 1620, 3240, 3410, 3595, and 3650 cm⁻¹, although they vary in intensity. Moreover, the synthesized samples show two additional peaks at 910 and 1025 cm⁻¹ that are absent in the spectrum of the natural opal-AG.

The large band between 900 and 1100 cm⁻¹ encompasses several components, as revealed by multiple shoulders at 910, 970, and 1065 cm⁻¹, which are attributed to vibration modes of the silica structure [79–85]. The 1025 cm⁻¹ contribution regularly decreases in intensity from sample Op1:0 to Op1:2, and, hence, with increasing hydrogel proportion.

The broad and complex band between 3000 and 3700 cm⁻¹ is attributed to water and silanol groups in the literature [79,81,82,86,87]. It is also composed of several components, as revealed by several shoulders at 3240, 3410, 3595, and 3650 cm⁻¹. Its global shape varies between samples: the components at 3240 and 3410 cm⁻¹ dominate for Op1:0, Op1:1, and Op1:2, and the components at 3595 and 3650 cm⁻¹ dominate for Op1:0.5, inducing a softer slope between 3000 and 3500 cm⁻¹. In this area, the spectrum of the natural opal-AG is remarkably similar to that of sample Op1:1. The integrated area of this complex band between 3000 and 3700 cm⁻¹ (normalized to the 430 cm⁻¹ peak) varies, in decreasing order, as follows: 434 for Op1:2, 174 for Op1:1, 163 for Op1:0, and 85 for Op1:0.5. Hence, the more hydrogel in the synthesis, the more the water arrangements differ (except for Op1:0.5).

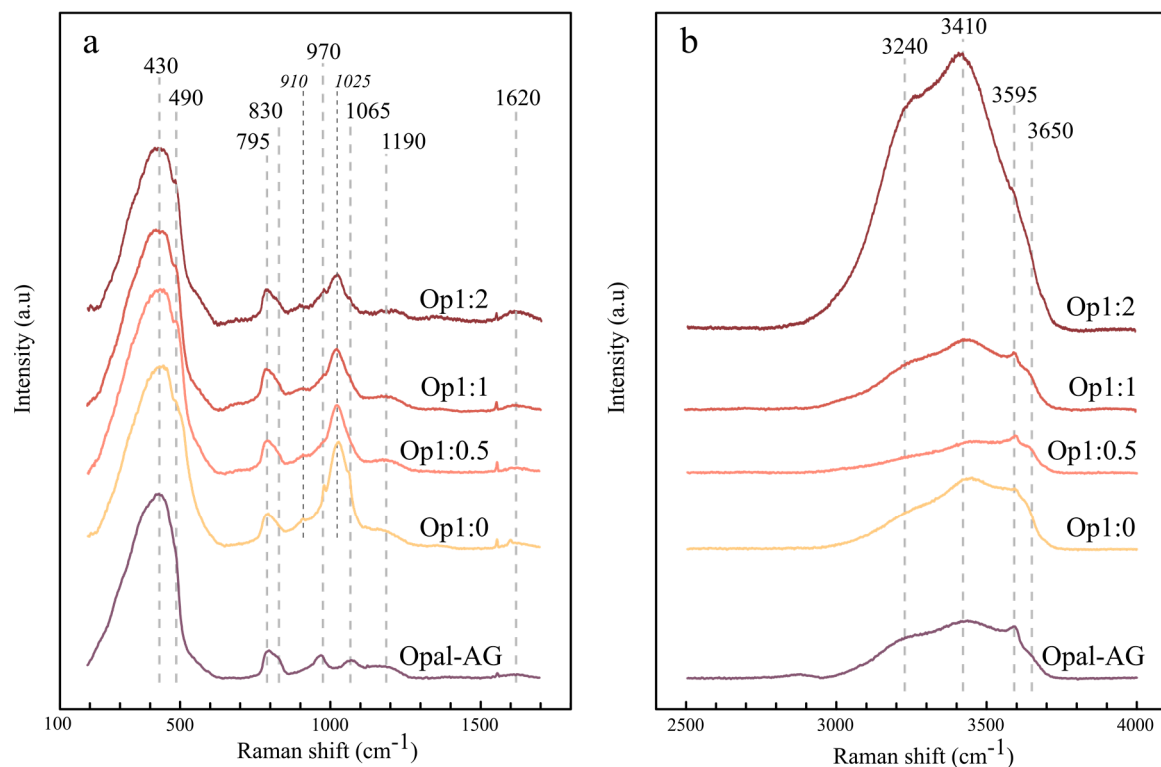


Figure 8. Raman spectra of the four synthetic opals and one natural white opal-A. (a) Silica structure region (100–1700 cm^{-1}); (b) water region (2500–4000 cm^{-1}).

4. Discussion

4.1. Synthesized Products: Opal-A Analogs

4.1.1. Atomic Structure

The Raman spectra in Figure 8 show that our synthetic opals present the same broad band at 430 cm^{-1} (bending Si-O vibration) and at 795 cm^{-1} (symmetric stretching Si-O vibration) as the natural opal-A [88,89]. By analogy with natural opals, the complex region between 900 and 1000 cm^{-1} in our product can be assigned to a mix of stretching vibrations from silanols and Si-O for Q^1 and Q^2 units [82]. The band at 970 cm^{-1} is related to the stretching of silanols linked to the silica structure [88–91]. The intensity of this signal is the highest in Op1:0, without hydrogel solution, which possesses the largest pores, and the lowest in Op1:2, which contains twice more hydrogel solution than nanograin solution. A larger pore size may induce more silanol groups in the terminating position and, therefore, an increase in their number in the atomic structure. This could explain why Op1:0 shows a more intense signal of the 970 cm^{-1} band. This contribution can be linked to the 490 cm^{-1} shoulder, as the latter is the signature of defect-like structural features in the atomic structure caused by silanols [92]. The peaks at 910 , 1065 , and 1190 cm^{-1} are related to the stretching vibration of Si-O for Q^2 , Q^3 , and Q^4 units respectively [79–84]. The peak at 910 cm^{-1} , clearly visible in all the syntheses, may reflect a higher relative abundance of Q^2 units in their silica structure than in natural opals. Finally, the intense band at 1025 cm^{-1} is observed only in the spectra of synthetic samples and absent in natural ones. We propose two interpretations for this band. First, the KOH pellets we used for the method display a sharp Raman peak at 1050 cm^{-1} (Figure S1). Hence, the 1025 cm^{-1} band may be due to KOH nanoparticles deposited within the porosity of our synthetic opal. The shift in position, which is concomitant with the broadening, is typical of the commonly observed Raman signal evolution with crystal size diminution. Second, this 1050 cm^{-1} band has been attributed in the infrared either to dimer (Si_2O_7) or to HSiO_3^- [6], but it has not yet been observed in similar materials by Raman spectroscopy. The juvenility of the synthesized products compared to the natural ones may explain why the bands at 910 (and possibly the

one at 1025 cm^{-1}) show dissimilarities between the synthetic and the natural samples. In nature, opal may benefit from the ageing effect induced by a long timescale of formation and residence, allowing the progressive reorganization of the silica network [93]. This could lead to a diminution in Q^1 and Q^2 and a concomitant increase in Q^3 and Q^4 , as well as the disappearance of the 1025 cm^{-1} band due to the polymerization of the overall atomic structure. In this hypothesis, the 1025 cm^{-1} band would be ascribed to HSiO_3^- rather than to Si_2O_7 , the latter indicating an already high order of polymerization. Another example of opal transformation with time is the development of cracks in opal due to internal atomic re-arrangement [94]. This juvenility may also explain why the synthetic sample that did not require HF treatment was not required for SEM observation of the structure, when it is usually required for natural samples, which are much older.

4.1.2. Nano- to Micro-Structure

All the synthetic opals we obtained are mesoporous. They show rounded silica nanograins, 25 to 40 nm in diameter, which are randomly arranged (Figure 6) and cemented by silica hydrogel. By increasing the volume of the hydrogel, large mesopores are progressively filled: the mean pore size progressively decreased from 20 nm down to 4 nm (with the exception of sample Op1:1, which still shows a major large pore contribution on BJH, possibly due to local heterogeneities in the sample). This suggests that the hydrogel gradually spreads over the surfaces of the large pores, thus reducing their size. This hypothesis is consistent with the observed macroscopic behavior of the samples when they are immersed in water: the smaller the pores, the longer it takes for water to enter them. In addition, the pore size in all our synthetic opals is consistent with the porosity of natural opals, which varies between approximately 1.5 and 10 nm, independently of the type of opal [4,5].

All the samples show some degree of nanograin aggregation, with protosphere structures (100–300 nm) composed of merged nanograins, cemented by the hydrogel (Figure 6). Such structures are consistent with those of natural opal-A [8]. More specifically, they correspond to that of common opal-AG (disordered nanograins assembly) much more than that of opal-AN [8]. The latter also displays a macroscopic botryoidal morphology that our synthetic opals do not display (Figure 4). This structure of opal-AG therefore possibly represents the early stage of the large spherical sur-structure typical of many natural opal-AGs. As shown by the DLS measurements (Figure 3) performed before the hydrogel incorporation, the formation of protospheres is first initiated, to a small extent, during the growing step in our experiment. However, we observe on SEM images (performed on the final, solid product) that the nanograins were mostly aggregated into protospheres (and not individual grains embedded in the hydrogel). This suggests that the majority of the protospheres formed during the incorporation of the hydrogel cement. We also show that the changes in hydrogel amount do not affect the proportions of nanograins or protospheres in the synthetic opals. However, we show that the changes in pH (from 13.5 to 10.5 in our experiment) affect the formation of these structures.

The studies conducted by Depasse and Watillon and by Iler [42,95] indicate that a decrease in pH below 11 results in a modification of the chemical function of potassium, which turns from a non-bridging into a bridging ion. The surfaces of the silica nanograins covered by acid groups form acid–base bonds with potassium, which subsequently leads to the coagulation of the silica nanograins into aggregates. The rate of aggregation by coagulation is proportional to the surface area of the silica per unit of volume. Consequently, particles or aggregates with greater surface areas are more likely to aggregate smaller grains. Furthermore, the uneven distribution of potassium on the surfaces of silica nanograins may induce an attraction between the nanograins, resulting in the aggregation of particles [96]. The aggregates that are formed by our method exhibit a rounded shape (Figure 6), indicating that coagulation occurred in suspension in the mixed solution before deposition by gravity (rather than in layers at the bottom of the beaker). Upon cessation of the agitation of the mixed solution, the protospheres settled by gravity at the bottom of the beaker, thereby stopping their growth by coagulation.

The structure of natural opal is therefore probably controlled by variations of intensive conditions (pH and temperature) that affect the ion properties and interactions with the silica matrix.

4.1.3. Chemistry

The chemical composition of three of our products (Op1:0, Op1:0,5 and Op1:1) is consistent with the typical composition of natural opals, which features between 2 and 18 wt% H₂O [1–5].

By contrast, Op1:2 is richer in water content (34 wt%) and less rich in silica (62 wt%) (Table 3). These values are less consistent with those of natural opals. This may indicate that in nature, the ratio between the hydrogel cement and the nanograins should not exceed 1:1. The formation of a hydrogel cement would therefore be a ‘final stage’ in nature, taking place in the spaces left by the nanograins and their aggregated structures, formed previously.

The water concentration seems to be somehow linked to the amount of hydrogel cement incorporated in the sample. Concomitantly, the more hydrogel solution is added during synthesis, the lower the concentrations of potassium and silicon. It can thus be proposed that increases in the water amount lower the concentrations of silicon and potassium by a dilution effect: the silica content dropped from 85 ± 1.2 wt% down to 62.2 ± 0.7 wt%, and the potassium content dropped from 6.1 ± 0.1 wt% down to 1.8 ± 0.2 wt% for samples Op1:0 and Op1:2, respectively.

The potassium concentration is much higher in the synthetic samples (3 to 6 wt%) than in the natural opals, in which it does not exceed 1 wt% [14,69]. However, potassium being the only chemical element introduced during the synthesis, its concentration fits well with the sum of the impurities (Al, Ca, Na, K) in natural opal, typically ranging from 1 to 6 wt% [14,69].

In nature, opal chemistry is strongly influenced by the crystallization of other phases in the fluid if some elements reach saturation prior to opal formation. Opal hence incorporates the ‘leftovers’. These probably interact with the silica monomers and influence the nanograin’s formation and aggregated structures. These relationships between chemistry and structure are certainly to be considered further. After the study by Iler (1979), who investigated opal formation in conditions irrelevant to natural processes, further studies deserve to be conducted on the role of additional cations (Al, Ca, Na. . .) in the structure of geologically relevant synthetic opal.

4.1.4. Water State

The Raman spectra in Figure 8 show that our synthetic opals display the typical bands of molecular water (H₂O) at 1620 cm^{-1} (bending) and at $3240\text{--}3410\text{ cm}^{-1}$ (stretching) [79,81,82,86,87]. The 3595 cm^{-1} band has been ascribed to silanol vibration [91,97]. Finally, the 3650 cm^{-1} shoulder corresponds to the stretching vibration of silanol [91]. All these spectral features are displayed similarly in the spectrum of the natural opal-A.

The nitrogen adsorption–desorption results suggest that increasing the volume ratio of the hydrogel induces a gradual filling of the large pores (Figure 7). The amount of water incorporated in the synthesis, both measured by LOD (Table 2) and estimated by Raman spectroscopy (Figure 8), correlates with the increase in the volume ratio of the hydrogel (Figure 9), with the exception of Op1:0. In particular, Op1:2 was synthesized with four times more hydrogel than Op1:0.5 and also contains roughly four times more water and a Raman water signal nearly four times more intense than that of Op1:0.5. This may suggest that in natural opals, water would be incorporated preferentially in the silica gel cementing the nanograins and aggregated structures. This merits further investigation into natural opals.

The case of Op1:0 (without any hydrogel) is different. This sample shows a rather high-water content (9.02 ± 0.1 wt%), as well as a rather intense Raman water signal, both of which are higher than the equivalent values in Op1:0.5 (Figure 9). This may indicate that the water present in Op1:0 is incorporated in a different manner from the three other synthetic samples (Op1:0.5, Op1:1 and Op1:2). The surface charge from silica particle

surfaces, as well as confined nanopores, have been shown to be able to adsorb water in significant proportions [98–100]. The significant amount of water present in Op1:0 and the decreased water amount in Op1:0.5 suggest that the cement is likely to be replacing the pore water between the silica nanograins. We note that Op1:0 displays the largest pores in our sample set. We suggest that the abundance of large pores would favor the adsorption of free water, despite the absence of hydrogel.

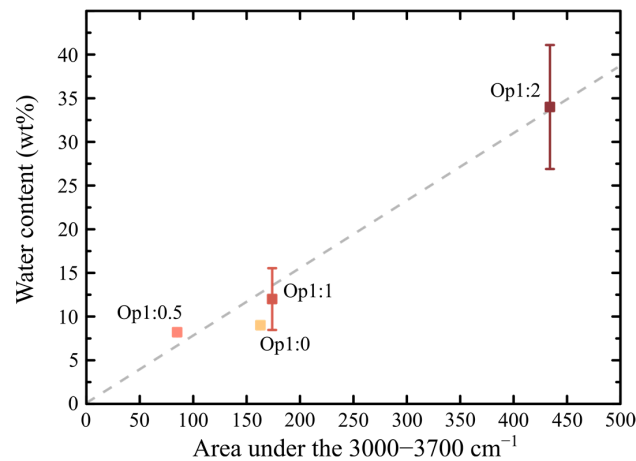


Figure 9. Plot of the water content measured by LOD versus the area under the water Raman band. The dashed, gray line is the correlation trend excluding Op1:0 (see text for details).

In accordance with all the points discussed above, we propose, in Figure 10, a schematic drawing of the repartition of water (H_2O and OH) in our samples, modified after the previous work by Day and Jones (2008) [101].

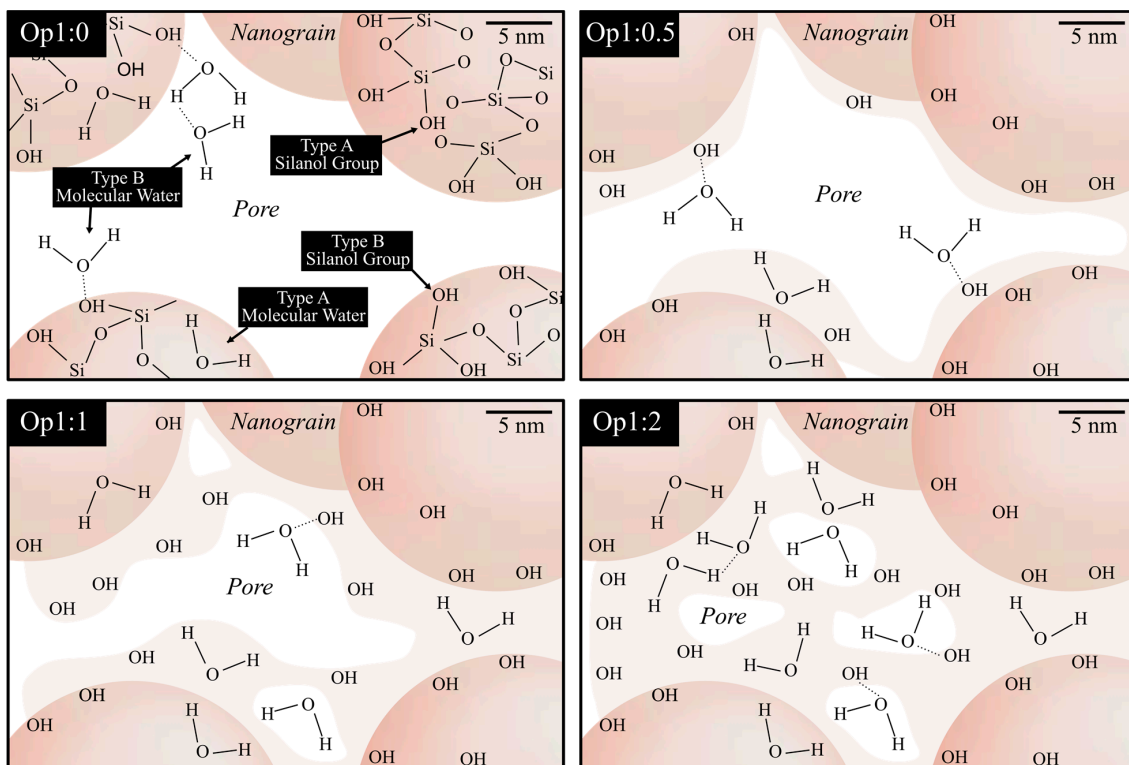


Figure 10. Hypothetical water distribution (H_2O and silanols) in our four synthetic samples, based on the previous work of Day and Jones (2008) [101], constrained by the results of Raman spectroscopy, loss on drying, and gas adsorption.

4.2. Implications for Terrestrial Opal

Our experiment was designed to simulate many of the parameters believed to occur during natural opal formation. The 20–50 °C temperature range is consistent with most continental weathering systems, where opal forms in groundwater [19–27]. It is also consistent with the lowest temperatures observed in hydrothermal systems [29–35]. We used water as the only solvent, which is consistent with all that is known about terrestrial opal. We also avoided the use of irrelevant organic chemicals used in other opal synthesis methods, such as methanol or tetraethyl orthosilicate (TEOS), as these are rarely or never encountered in nature. However, we concede several exceptions, detailed below:

- We used anomalously high pH thanks to a KOH solution. Thanks to this, we obtained significant yields in reasonable times, which allowed the structural and physical characterization of the final solid product.
- We used potassium as the only chemical impurity in the system, although many others occur in nature, aluminum in particular [26,69,102–105].

We now plan to adjust our synthesis method toward more geologically relevant conditions, lower-pH conditions and the effect of the incorporation of chemical impurities (e.g., Al, Ca, Na...), in order to study the effect of such conditions on opal formation and properties.

From the observation standpoint, natural opal is a composite material, made of aggregated silica grains cemented within hydrogel. For this reason, we elaborated a synthesis method in three steps: first, the formation of silica nanograins; second, the formation of hydrogel; and third, the mixing of both to favor aggregation. The structural results shown in the SEM images (Figures 5 and 6) are satisfactorily similar to those obtained for natural common opal-AG [8]. This may suggest that this three-step mechanism has some natural relevance, although these steps may well overlap in nature. Our structural results also suggest that, in nature, the cementation step takes place only after the formation, aggregation, and deposition of the nanograins, and that it is limited to the space between them.

4.3. Implications for Martian Opal

Opal is a common alteration product on Mars [106]. From orbit, it has been found over a wide range of latitudes and elevations, and it pertains to terrains ranging from the Noachian era (4.1–3.7 Ga) to, possibly, the Amazonian (<3 Ga). As far as is allowed by the orbital remote sensing of the mineralogy and geology, opals in various hydration and crystallinity states have been found, including opal-A, opal-CT, and chalcedony [71,107]. Based on the opal spectral features from near-infrared reflectance spectroscopy, the mineral associations, and the geomorphic evidence, some sites have been linked to low-temperature hydrothermal activity and impact-induced hydrothermal systems. Others have been linked to acid–fog weathering, pedogenic sequences, silcrete coatings, or even direct precipitation in bodies of water associated with alluvial fans and deltas [108]. Non-terrestrial geological settings may also have occurred. Opal-A, with 3–6 wt% H₂O, has been found in situ by several rover missions in the form of, for example, diagenetic halos, attesting to groundwater circulation in lakebed sediments in Gale crater [70,109]. Despite this wealth of discoveries, critical outstanding questions for Mars opals that remain particularly because the formation of opal on Earth itself remains somehow elusive. As our study is a step toward a better understanding of opal formation, this may also help to understand its formation on Mars. We propose to use this experimental work as a framework to reproduce opal formation in more Mars-relevant conditions, such as by using CO₂-rich fluids.

5. Conclusions

We have developed a method for the synthesis of common opal-AG under geologically relevant conditions (<50 °C, ambient pressure, and realistic chemicals) in order to document the steps in its formation and explore the effect of various constituents' proportions on opal properties. The synthesis method was designed to try to reproduce the supposed natural process of opal formation in water: first, we produced silica nanograins 25 to 40 nm in

diameter, considered as the building blocks of the opal structure, and second, we cemented these nanograins and their aggregates (e.g., spheres) using a silica hydrogel cement. Four different synthetic opals were prepared with various mixing ratios between nanograins and silica hydrogel: Op1:0 (without hydrogel), Op1:0.5, Op1:1, and Op1:2 (with hydrogel constituting two-thirds of the volume of the product). We obtained the most relevant results from Op1:1, which exhibited Raman properties (both in the Si-O-Si region and in the water region), silica and water content (84 and 12 wt%, respectively), silica nanograin sizes, and pore sizes that are the closest to those of natural opal-AG. A higher hydrogel content (Op1:2) provides unrealistic water content (34 wt%), and no hydrogel content (Op1:0), forming a structurally irrelevant analogue. This may indicate that in nature, the formation of a hydrogel cement would be a systematic ‘final stage’, with the cement filling in the spaces left by the nanograins and aggregates previously formed.

As show by the correlation between our results, an increase in the hydrogel content in opal (1) increases the porous volume from 0.2 to 0.39, (2) decreases the size of the pores from 20 to 4 nm, and (3) increases the overall water content from 8 to 34 wt% (for both molecular water and chemically bonded silanol). This suggests that water is preferentially located in the cement (hydrogel) rather than in the nanograins. This may have implications for the understanding of the durability and ageing phenomena of opal in nature, particularly the fact that water remains in the opal structure for long times in arid and cold environments, such as on Mars.

Further experiments, such as ^{29}Si Nuclear Magnetic Resonance (NMR) and infrared spectroscopy (IR) investigations, may help to obtain a more insightful characterization of Q^n and water states in this synthetic product and its comparison with natural samples. For a better understanding of opal formation in nature, the synthesis of opals with the incorporation of additional impurities, such as Al and Ca, both relevant to natural opals, must now be achieved by adapting the method presented here.

Supplementary Materials: The following supporting information can be downloaded at: <https://www.mdpi.com/article/10.3390/min14100969/s1>. Figure S1: Raman spectra comparison between Op1:1 and KOH pellet.

Author Contributions: Conceptualization, S.G., B.R., V.V. and B.C.; methodology S.G., B.R., V.V. and B.C.; validation, V.V., B.C., M.-V.C. and J.C.; formal analysis, S.G.; investigation, S.G., M.-V.C., H.T. and O.G.; resources, B.R., V.V. and J.C.; data curation, S.G.; writing—original draft preparation, S.G. and B.R.; writing—review and editing, V.V., B.C., M.-V.C. and J.C.; visualization, S.G.; supervision, B.C., V.V. and J.C.; project administration, J.C.; funding acquisition, J.C. All authors have read and agreed to the published version of the manuscript.

Funding: This research was funded by the Agence Nationale de la Recherche (ANR, France), grant PALEOSILICA ANR-20-CE49-0013.

Data Availability Statement: Dataset available on request from the authors.

Acknowledgments: We extend our warmest thanks to the 10 anonymous reviewers, who particularly helped to consolidate this paper. We thank Laurent Lenta for his help in sample preparation; Marion Rivoal and Carole La for the management of ICP-MS and LOD measurements (all three at the Laboratoire de Planétologie et Géosciences, Nantes); and Nicolas Stephant (Institut des Matériaux Jean Rouxel, Nantes) for his help in SEM operations.

Conflicts of Interest: The authors declare no conflicts of interest.

References

1. Segnit, E.R.; Stevens, T.J.; Jones, J.B. The Role of Water in Opal. *J. Geol. Soc. Aust.* **1965**, *12*, 211–226. [[CrossRef](#)]
2. Jones, J.B.; Segnit, E.R. The Nature of Opal I. Nomenclature and Constituent Phases. *J. Geol. Soc. Aust.* **1971**, *18*, 57–68. [[CrossRef](#)]
3. Langer, K.; Flörke, O.W. Near Infrared Absorption Spectra (4000–9000 cm^{-1}) of Opals and the Role of “Water” in the $\text{SiO}_2\text{nH}_2\text{O}$ Minerals. *Fortschritte Mineral.* **1974**, *52*, 17–51.
4. Thomas, P.; Chauviré, B.; Flower-Donaldson, K.; Aldridge, L.; Smallwood, A.; Liu, B. FT-NIR and DSC Characterisation of Water in Opal. *Ceram. Int.* **2020**, *46*, 29443–29450. [[CrossRef](#)]

5. Chauviré, B.; Thomas, P.S. DSC of Natural Opal: Insights into the Incorporation of Crystallisable Water in the Opal Microstructure. *J. Therm. Anal. Calorim.* **2020**, *140*, 2077–2085. [[CrossRef](#)]
6. Guthrie, G.D.; Dish, D.L.; Reynolds, R.C., Jr. Modeling the X-ray Diffraction Pattern of Opal-CT. *Am. Mineral.* **1995**, *80*, 869–872. [[CrossRef](#)]
7. Elzea, J.M.; Rice, S.B. TEM and X-Ray Diffraction Evidence for Cristobalite and Tridymite Stacking Sequences in Opal. *Clays Clay Miner.* **1996**, *44*, 492–500. [[CrossRef](#)]
8. Gaillou, E.; Fritsch, E.; Aguilar-Reyes, B.; Rondeau, B.; Post, J.; Barreau, A.; Ostroumov, M. Common Gem Opal: An Investigation of Micro- to Nano-Structure. *Am. Mineral.* **2008**, *93*, 1865–1873. [[CrossRef](#)]
9. Wilson, M.J. The Structure of Opal-CT Revisited. *J. Non-Cryst. Solids* **2014**, *405*, 68–75. [[CrossRef](#)]
10. Fröhlich, F. The Opal-CT Nanostructure. *J. Non-Cryst. Solids* **2020**, *533*, 119938. [[CrossRef](#)]
11. Smallwood, A.G.; Thomas, P.S.; Ray, A.S. Characterisation of Sedimentary Opals by Fourier Transform Raman Spectroscopy. *Spectrochim. Acta Part. A Mol. Biomol. Spectrosc.* **1997**, *53*, 2341–2345. [[CrossRef](#)]
12. Ostroumov, M.; Fritsch, E.; Lasnier, B.; Lefrant, S. Spectres Raman Des Opales: Aspect Diagnostique et Aide a La Classification. *Eur. J. Mineral.* **1999**, *11*, 899–908. [[CrossRef](#)]
13. Adamo, I. A Contribution to the Study of FTIR Spectra of Opals. *Neues Jahrb. Für Mineral.-Abh. J. Mineral. Geochem.* **2010**, *187*, 63–68. [[CrossRef](#)]
14. Chauviré, B.; Rondeau, B.; Mangold, N. Near Infrared Signature of Opal and Chalcedony as a Proxy for Their Structure and Formation Conditions. *Eur. J. Mineral.* **2017**, *29*, 409–421. [[CrossRef](#)]
15. Curtis, N.J.; Gascooke, J.R.; Johnston, M.R.; Pring, A. A Review of the Classification of Opal with Reference to Recent New Localities. *Minerals* **2019**, *9*, 299. [[CrossRef](#)]
16. Curtis, N.J.; Gascooke, J.R.; Pring, A. Silicon-Oxygen Region Infrared and Raman Analysis of Opals: The Effect of Sample Preparation and Measurement Type. *Minerals* **2021**, *11*, 173. [[CrossRef](#)]
17. Curtis, N.J.; Gascooke, J.R.; Johnston, M.R.; Pring, A. ²⁹Si Solid-State NMR Analysis of Opal-AG, Opal-AN and Opal-CT: Single Pulse Spectroscopy and Spin-Lattice T1 Relaxometry. *Minerals* **2022**, *12*, 323. [[CrossRef](#)]
18. Webster, R. *Gems: Their Sources, Descriptions and Identification*; Butterworth and Co. Publishers: Oxford, UK, 1975.
19. Summerfield, M.A. Origin and Palaeoenvironmental Interpretation of Sarsens. *Nature* **1979**, *281*, 137–139. [[CrossRef](#)]
20. Summerfield, M.A. Silcrete as a Palaeoclimatic Indicator: Evidence from Southern Africa. *Palaeogeogr. Palaeoclimatol. Palaeoecol.* **1983**, *41*, 65–79. [[CrossRef](#)]
21. Thiry, M.; Millot, G. Mineralogical Forms of Silica and Their Sequence of Formation in Silcretes. *J. Sediment. Res.* **1987**, *57*, 343–352. [[CrossRef](#)]
22. Milnes, A.R.; Wright, M.J.; Thiry, M. Silica Accumulations in Saprolites and Soils in South Australia. *Occur. Charact. Genes. Carbonate Gypsum Silica Accumul. Soils* **1991**, *26*, 121–149. [[CrossRef](#)]
23. Thiry, M.; Simon-Coinçon, R. Tertiary Paleoweatherings and Silcretes in the Southern Paris Basin. *CATENA* **1996**, *26*, 1–26. [[CrossRef](#)]
24. Ulyyott, J.S.; Nash, D.J.; Whiteman, C.A.; Mortimore, R.N. Distribution, Petrology and Mode of Development of Silcretes (Sarsens and Puddingstones) on the Eastern South Downs, UK. *Earth Surf. Process. Landf.* **2004**, *29*, 1509–1539. [[CrossRef](#)]
25. Thiry, M.; Milnes, A.R.; Rayot, V.; Simon-Coinçon, R. Interpretation of Palaeoweathering Features and Successive Silicifications in the Tertiary Regolith of Inland Australia. *JGS* **2006**, *163*, 723–736. [[CrossRef](#)]
26. Rondeau, B.; Cenko-Tok, B.; Fritsch, E.; Mazzero, F.; Gauthier, J.-P.; Bodeur, Y.; Bekele, E.; Gaillou, E.; Ayalew, D. Geochemical and Petrological Characterization of Gem Opals from Wegel Tena, Wollo, Ethiopia: Opal Formation in an Oligocene Soil. *Geochem. Explor. Environ. Anal.* **2012**, *12*, 93–104. [[CrossRef](#)]
27. Chauviré, B.; Rondeau, B.; Alexandre, A.; Chamard-Bois, S.; La, C.; Mazzero, F. Pedogenic Origin of Precious Opals from Wegel Tena (Ethiopia): Evidence from Trace Elements and Oxygen Isotopes. *Appl. Geochem.* **2019**, *101*, 127–139. [[CrossRef](#)]
28. Arnórsson, S. The Use of Mixing Models and Chemical Geothermometers for Estimating Underground Temperatures in Geothermal Systems. *J. Volcanol. Geotherm. Res.* **1985**, *23*, 299–335. [[CrossRef](#)]
29. Herzig, P.M.; Becker, K.P.; Stoffers, P.; Bäcker, H.; Blum, N. Hydrothermal Silica Chimney Fields in the Galapagos Spreading Center at 86°W. *Earth Planet. Sci. Lett.* **1988**, *89*, 261–272. [[CrossRef](#)]
30. Lalou, C. Deep-Sea Hydrothermal Venting: A Recently Discovered Marine System. *J. Mar. Syst.* **1991**, *1*, 403–440. [[CrossRef](#)]
31. Jones, B.; Renaut, R.W. Hot Spring and Geyser Sinters: The Integrated Product of Precipitation, Replacement, and Deposition. *Can. J. Earth Sci.* **2003**, *40*, 1549–1569. [[CrossRef](#)]
32. Goryniuk, M.C.; Rivard, B.A.; Jones, B. The Reflectance Spectra of Opal-A (0.5–25 Mm) from the Taupo Volcanic Zone: Spectra That May Identify Hydrothermal Systems on Planetary Surfaces. *Geophys. Res. Lett.* **2004**, *31*. [[CrossRef](#)]
33. Channing, A.; Butler, I.B. Cryogenic Opal-A Deposition from Yellowstone Hot Springs. *Earth Planet. Sci. Lett.* **2007**, *257*, 121–131. [[CrossRef](#)]
34. Barnes, J.D.; Paulick, H.; Sharp, Z.D.; Bach, W.; Beaudoin, G. Stable Isotope ($\delta^{18}\text{O}$, δD , $\delta^{37}\text{Cl}$) Evidence for Multiple Fluid Histories in Mid-Atlantic Abyssal Peridotites (ODP Leg 209). *Lithos* **2009**, *110*, 83–94. [[CrossRef](#)]
35. Campbell, K.A.; Guido, D.M.; Gautret, P.; Foucher, F.; Ramboz, C.; Westall, F. Geyselite in Hot-Spring Siliceous Sinter: Window on Earth's Hottest Terrestrial (Paleo)Environment and Its Extreme Life. *Earth-Sci. Rev.* **2015**, *148*, 44–64. [[CrossRef](#)]

36. Rey, P.F. Opalisation of the Great Artesian Basin (Central Australia): An Australian Story with a Martian Twist. *Aust. J. Earth Sci.* **2013**, *60*, 291–314. [[CrossRef](#)]
37. Staatz, M.H.; Bauer, H.L., Jr. *Virgin Valley Opal District, Humboldt County, Nevada*; U.S. Geological Survey: Reston, VA, USA, 1951. [[CrossRef](#)]
38. Koivula, J.I.; Fryer, C.; Keller, P.C. Opal from Querétaro, Mexico: Occurrence and Inclusions. *Gems Gemol.* **1983**, *19*, 87–96. [[CrossRef](#)]
39. Spencer, R.J.; Levinson, A.A.; Koivula, J.I. Opal from Querétaro, Mexico: Fluid Inclusion Study. *Gems Gemol.* **1992**, *28*, 28–34. [[CrossRef](#)]
40. Townsend, I.J. The Geology of Australian Opal Deposits. *Aust. Gemol.* **2001**, *21*, 34–37.
41. Ayalew, D.; Pik, R.; Gibson, S.; Yirgu, G.; Ali, S.; Assefa, D. Pedogenic Origin of Mezezo Opal Hosted in Ethiopian Miocene Rhyolites. *Can. Mineral.* **2020**, *58*, 231–246. [[CrossRef](#)]
42. Iler, R.K. *The Chemistry of Silica, Solubility, Polymerization. Colloid. and Surface Properties, and Biochemistry*; Wiley-Interscience: New York, NY, USA, 1979; ISBN 978-0-471-02404-0.
43. Tobler, D.J.; Shaw, S.; Benning, L.G. Quantification of Initial Steps of Nucleation and Growth of Silica Nanoparticles: An in-Situ SAXS and DLS Study. *Geochim. Cosmochim. Acta* **2009**, *73*, 5377–5393. [[CrossRef](#)]
44. Tobler, D.J.; Benning, L.G. In Situ and Time Resolved Nucleation and Growth of Silica Nanoparticles Forming under Simulated Geothermal Conditions. *Geochim. Cosmochim. Acta* **2013**, *114*, 156–168. [[CrossRef](#)]
45. Smoluchowski, M. Mathematical Theory of the Kinetics of the Coagulation of Colloidal Solutions. *Z. Für Phys. Chem.* **1917**, *19*, 129–135.
46. Darragh, P.J.; Gaskin, A.J.; Terrell, B.C.; Sanders, J.V. Origin of Precious Opal. *Nature* **1966**, *209*, 13–16. [[CrossRef](#)]
47. Salvarezza, R.C.; Vázquez, L.; Míguez, H.; Mayoral, R.; López, C.; Meseguer, F. Edward-Wilkinson Behavior of Crystal Surfaces Grown By Sedimentation of SiO₂ Nanospheres. *Phys. Rev. Lett.* **1996**, *77*, 4572–4575. [[CrossRef](#)]
48. Sanders, J.V. Colour of Precious Opal. *Nature* **1964**, *204*, 1151–1153. [[CrossRef](#)]
49. Stöber, W.; Fink, A.; Bohn, E. Controlled Growth of Monodisperse Silica Spheres in the Micron Size Range. *J. Colloid Interface Sci.* **1968**, *26*, 62–69. [[CrossRef](#)]
50. Yoshida, A. Silica Nucleation, Polymerization, and Growth Preparation of Monodispersed Sols. *Adv. Chem.* **1994**, *234*, 51–66.
51. Schlomach, J.; Kind, M. Investigations on the Semi-Batch Precipitation of Silica. *J. Colloid Interface Sci.* **2004**, *277*, 316–326. [[CrossRef](#)] [[PubMed](#)]
52. Tan, T.T.Y.; Liu, S.; Zhang, Y.; Han, M.Y.; Selvan, S.T. Microemulsion Preparative Methods (Overview). *Compr. Nanosci. Technol.* **2011**, *5*, 399–441. [[CrossRef](#)]
53. Rezaei, S.; Manoucheri, I.; Moradian, R.; Pourabbas, B. One-Step Chemical Vapor Deposition and Modification of Silica Nanoparticles at the Lowest Possible Temperature and Superhydrophobic Surface Fabrication. *Chem. Eng. J.* **2014**, *252*, 11–16. [[CrossRef](#)]
54. Nabil, M.; Motaweh, H.A. Silica Nanoparticles Preparation Using Alkali Etching Process. *Appl. Mech. Mater.* **2015**, *749*, 155–158. [[CrossRef](#)]
55. Nabil, M.; Mahmoud, K.R.; El-Shaer, A.; Nayber, H.A. Preparation of Crystalline Silica (Quartz, Cristobalite, and Tridymite) and Amorphous Silica Powder (One Step). *J. Phys. Chem. Solids* **2018**, *121*, 22–26. [[CrossRef](#)]
56. Awaji, N.; Ohkubo, S.; Nakanishi, T.; Aoyama, T.; Sugita, Y.; Takasaki, K.; Komiya, S. Thermal Oxide Growth at Chemical Vapor Deposited SiO₂/Si Interface during Annealing Evaluated by Difference X-ray Reflectivity. *Appl. Phys. Lett.* **1997**, *71*, 1954–1956. [[CrossRef](#)]
57. Jang, H.D. Experimental Study of Synthesis of Silica Nanoparticles by a Bench-Scale Diffusion Flame Reactor. *Powder Technol.* **2001**, *119*, 102–108. [[CrossRef](#)]
58. Cai, X.; Hong, R.Y.; Wang, L.S.; Wang, X.Y.; Li, H.Z.; Zheng, Y.; Wei, D.G. Synthesis of Silica Powders by Pressured Carbonation. *Chem. Eng. J.* **2009**, *151*, 380–386. [[CrossRef](#)]
59. Wu, Z.; Hu, X.; Tao, C.; Li, Y.; Liu, J.; Yang, C.; Shen, D.; Li, G. Direct and Label-Free Detection of Cholic Acid Based on Molecularly Imprinted Photonic Hydrogels. *J. Mater. Chem.* **2008**, *18*, 5452. [[CrossRef](#)]
60. Koay, N.; Burgess, I.B.; Kay, T.M.; Nerger, B.A.; Miles-Rossouw, M.; Shirman, T.; Vu, T.L.; England, G.; Phillips, K.R.; Utech, S.; et al. Hierarchical Structural Control of Visual Properties in Self-Assembled Photonic-Plasmonic Pigments. *Opt. Express* **2014**, *22*, 27750. [[CrossRef](#)]
61. Vazquez, N.I.; Gonzalez, Z.; Ferrari, B.; Castro, Y. Synthesis of Mesoporous Silica Nanoparticles by Sol–Gel as Nanocontainer for Future Drug Delivery Applications. *Boletín Soc. Española Cerámica Y Vidr.* **2017**, *56*, 139–145. [[CrossRef](#)]
62. Rothbaum, H.P.; Rohde, A.G. Kinetics of Silica Polymerization and Deposition from Dilute Solutions between 5 and 180°C. *J. Colloid Interface Sci.* **1979**, *71*, 533–559. [[CrossRef](#)]
63. Icopini, G.A.; Brantley, S.L.; Heaney, P.J. Kinetics of Silica Oligomerization and Nanocolloid Formation as a Function of pH and Ionic Strength at 25 °C. *Geochim. Cosmochim. Acta* **2005**, *69*, 293–303. [[CrossRef](#)]
64. Conrad, C.F.; Icopini, G.A.; Yasuhara, H.; Bandstra, J.Z.; Brantley, S.L.; Heaney, P.J. Modeling the Kinetics of Silica Nanocolloid Formation and Precipitation in Geologically Relevant Aqueous Solutions. *Geochim. Cosmochim. Acta* **2007**, *71*, 531–542. [[CrossRef](#)]
65. Scott, S.; Galeczka, I.M.; Gunnarsson, I.; Arnórsson, S.; Stefánsson, A. Silica Polymerization and Nanocolloid Nucleation and Growth Kinetics in Aqueous Solutions. *Geochim. Cosmochim. Acta* **2024**, *371*, 78–94. [[CrossRef](#)]

66. Gunnarsson, I.; Rsson, S.N.A. Amorphous Silica Solubility and the Thermodynamic Properties of H₄SiO₄ in the Range of 0° to 350 °C at Psat. *Geochim. Cosmochim. Acta* **2000**, *64*, 2295–2307. [[CrossRef](#)]
67. Gunnarsson, I.; Arnórsson, S. Impact of Silica Scaling on the Efficiency of Heat Extraction from High-Temperature Geothermal Fluids. *Geothermics* **2005**, *34*, 320–329. [[CrossRef](#)]
68. Van Den Heuvel, D.B.; Gunnlaugsson, E.; Gunnarsson, I.; Stawski, T.M.; Peacock, C.L.; Benning, L.G. Understanding Amorphous Silica Scaling under Well-Constrained Conditions inside Geothermal Pipelines. *Geothermics* **2018**, *76*, 231–241. [[CrossRef](#)]
69. Gaillou, E.; Delaunay, A.; Rondeau, B.; Bouhnik-le-Coz, M.; Fritsch, E.; Cornen, G.; Monnier, C. The Geochemistry of Gem Opals as Evidence of Their Origin. *Ore Geol. Rev.* **2008**, *34*, 113–126. [[CrossRef](#)]
70. Rapin, W.; Chauviré, B.; Gabriel, T.S.J.; McAdam, A.C.; Ehlmann, B.L.; Hardgrove, C.; Meslin, P.-Y.; Rondeau, B.; Dehouck, E.; Franz, H.B.; et al. In Situ Analysis of Opal in Gale Crater, Mars. *JGR Planets* **2018**, *123*, 1955–1972. [[CrossRef](#)]
71. Pineau, M.; Le Deit, L.; Chauviré, B.; Carter, J.; Rondeau, B.; Mangold, N. Toward the Geological Significance of Hydrated Silica Detected by near Infrared Spectroscopy on Mars Based on Terrestrial Reference Samples. *Icarus* **2020**, *347*, 113706. [[CrossRef](#)]
72. Tsai, M.-S. The Study of Formation Colloidal Silica via Sodium Silicate. *Mater. Sci. Eng. B* **2004**, *106*, 52–55. [[CrossRef](#)]
73. Matsoukas, T.; Gulari, E. Monomer-Addition Growth with a Slow Initiation Step: A Growth Model for Silica Particles from Alkoxides. *J. Colloid Interface Sci.* **1989**, *132*, 13–21. [[CrossRef](#)]
74. Qomariyah, L.; Sasmita, F.N.; Novaldi, H.R.; Widiyastuti, W.; Winardi, S. Preparation of Stable Colloidal Silica with Controlled Size Nano Spheres from Sodium Silicate Solution. *IOP Conf. Ser. Mater. Sci. Eng.* **2018**, *395*, 012017. [[CrossRef](#)]
75. Sjöberg, S. Silica in Aqueous Environments. *J. Non-Cryst. Solids* **1996**, *196*, 51–57. [[CrossRef](#)]
76. Brunauer, S.; Emmett, P.H.; Teller, E. Adsorption of Gases in Multimolecular Layers. *J. Am. Chem. Soc.* **1938**, *60*, 309–319. [[CrossRef](#)]
77. Barrett, E.P.; Joyner, L.G.; Halenda, P.P. The Determination of Pore Volume and Area Distributions in Porous Substances. I. Computations from Nitrogen Isotherms. *J. Am. Chem. Soc.* **1951**, *73*, 373–380. [[CrossRef](#)]
78. Jochum, K.P.; Weis, U.; Schwager, B.; Stoll, B.; Wilson, S.A.; Haug, G.H.; Andreae, M.O.; Enzweiler, J. Reference Values Following ISO Guidelines for Frequently Requested Rock Reference Materials. *Geostand. Geoanalytical Res.* **2016**, *40*, 333–350. [[CrossRef](#)]
79. Brawer, S.A.; White, W.B. Raman Spectroscopic Investigation of the Structure of Silicate Glasses. I. The Binary Alkali Silicates. *J. Chem. Phys.* **1975**, *63*, 2421–2432. [[CrossRef](#)]
80. Virgo, D.; Mysen, B.O.; Kushiro, I. Anionic Constitution of 1-Atmosphere Silicate Melts: Implications for the Structure of Igneous Melts. *Science* **1980**, *208*, 1371–1373. [[CrossRef](#)]
81. Mysen, B.O.; Virgo, D.; Seifert, F.A. The Structure of Silicate Melts: Implications for Chemical and Physical Properties of Natural Magma. *Rev. Geophys.* **1982**, *20*, 353–383. [[CrossRef](#)]
82. McMillan, P. Structural Studies of Silicate Glasses and Melts—Applications and Limitations of Raman Spectroscopy. *Am. Mineral.* **1984**, *69*, 622–644.
83. Rossano, S.; Mysen, B. Raman Spectroscopy of Silicate Glasses and Melts in Geological Systems. In *Raman Spectroscopy Applied to Earth Sciences and Cultural Heritage*; Ferraris, G., Dubessy, J., Caumon, M.-C., Rull, F., Eds.; European Mineralogical Union: London, UK, 2012; pp. 321–366. ISBN 978-0-903056-31-1. [[CrossRef](#)]
84. Le Losq, C.; Neuville, D.R. Effect of the Na/K Mixing on the Structure and the Rheology of Tectosilicate Silica-Rich Melts. *Chem. Geol.* **2013**, *346*, 57–71. [[CrossRef](#)]
85. Farfan, G.A.; McKeown, D.A.; Post, J.E. Mineralogical Characterization of Biosilicas versus Geological Analogs. *Geobiology* **2023**, *21*, 520–533. [[CrossRef](#)] [[PubMed](#)]
86. Matson, D.W.; Sharma, S.K.; Philpotts, J.A. The Structure of High-Silica Alkali-Silicate Glasses. A Raman Spectroscopic Investigation. *J. Non-Cryst. Solids* **1983**, *58*, 323–352. [[CrossRef](#)]
87. Chabiron, A.; Pironon, J.; Massare, D. Characterization of Water in Synthetic Rhyolitic Glasses and Natural Melt Inclusions by Raman Spectroscopy. *Contrib. Mineral. Petrol.* **2004**, *146*, 485–492. [[CrossRef](#)]
88. Zarubin, D.P. The Two-Component Bands at about 4500 and 800 Cm⁻¹ in Infrared Spectra of Hydroxyl-Containing Silicas. Interpretation in Terms of Fermi Resonance. *J. Non-Cryst. Solids* **2001**, *286*, 80–88. [[CrossRef](#)]
89. Sodo, A.; Casanova Municchia, A.; Barucca, S.; Bellatreccia, F.; Della Ventura, G.; Butini, F.; Ricci, M.A. Raman, FT-IR and XRD Investigation of Natural Opals. *J. Raman Spectrosc.* **2016**, *47*, 1444–1451. [[CrossRef](#)]
90. Hartwig, C.M.; Rahn, L.A. Bound Hydroxyl in Vitreous Silica. *J. Chem. Phys.* **1977**, *67*, 4260–4261. [[CrossRef](#)]
91. McMillan, P.; Remmele, R.L. Hydroxyl Sites in SiO₂ Glass: A Note on Infrared and Raman Spectra. *Am. Mineral.* **1986**, *71*, 772–778.
92. Mulder, C.A.M.; Damen, A.A.J.M. The Origin of the “Defect” 490 Cm⁻¹ Raman Peak in Silica Gel. *J. Non-Cryst. Solids* **1987**, *93*, 387–394. [[CrossRef](#)]
93. Gouzy, S.; Rondeau, B.; Gaudin, P.; Louarn, G.; La, C.; Lebeau, T.; Vinogradoff, V.; Clodoré, L.; Chamard-Bois, S. Whitening of Fire Opal: Transformation of Silica in Soils. *Chem. Geol.* **2023**, *616*, 121237. [[CrossRef](#)]
94. Chauviré, B.; Mollé, V.; Guichard, F.; Rondeau, B.; Thomas, P.S.; Fritsch, E. Cracking of Gem Opals. *Minerals* **2023**, *13*, 356. [[CrossRef](#)]
95. Depasse, J.; Watillon, A. The Stability of Amorphous Colloidal Silica. *J. Colloid Interface Sci.* **1970**, *33*, 430–438. [[CrossRef](#)]
96. Vrij, A.; Sonntag, H.; Težak, B.; Kitchener, J.A.; Matijević, E.; Mysels, K.J.; Overbeek, J.T.G.; Corkill, J.M.; Goodman, J.F.; Fowkes, F.M.; et al. General Discussion. *Discuss. Faraday Soc.* **1966**, *42*, 60–68. [[CrossRef](#)]

97. Davis, K.M.; Tomozawa, M. An Infrared Spectroscopic Study of Water-Related Species in Silica Glasses. *J. Non-Cryst. Solids* **1996**, *201*, 177–198. [[CrossRef](#)]
98. Muster, T.H.; Prestidge, C.A.; Hayes, R.A. Water Adsorption Kinetics and Contact Angles of Silica Particles. *Colloids Surf. A Physicochem. Eng. Asp.* **2001**, *176*, 253–266. [[CrossRef](#)]
99. Ng, K.C.; Chua, H.T.; Chung, C.Y.; Loke, C.H.; Kashiwagi, T.; Akisawa, A.; Saha, B.B. Experimental Investigation of the Silica Gel–Water Adsorption Isotherm Characteristics. *Appl. Therm. Eng.* **2001**, *21*, 1631–1642. [[CrossRef](#)]
100. Ilgen, A.G.; Kabengi, N.; Leung, K.; Ilani-Kashkouli, P.; Knight, A.W.; Loera, L. Defining Silica–Water Interfacial Chemistry under Nanoconfinement Using Lanthanides. *Environ. Sci. Nano* **2021**, *8*, 432–443. [[CrossRef](#)]
101. Day, R.; Jones, B. Variations in Water Content in Opal-A and Opal-CT from Geyser Discharge Aprons. *J. Sediment. Res.* **2008**, *78*, 301–315. [[CrossRef](#)]
102. Brown, L.D.; Ray, A.S.; Thomas, P.S. Elemental Analysis of Australian Amorphous Banded Opals by Laser-Ablation ICP-MS. *Neues Jahrb. Für Mineral.-Monatshefte* **2004**, *2004*, 411–424. [[CrossRef](#)]
103. McOrist, G.D.; Smallwood, A.; Fardy, J.J. Trace Elements in Australian Opals Using Neutron Activation Analysis. *J. Radioanal. Nucl. Chem. Artic.* **1994**, *185*, 293–303. [[CrossRef](#)]
104. McOrist, G.D.; Smallwood, A. Trace Elements in Coloured Opals Using Neutron Activation Analysis. *J. Radioanal. Nucl. Chem. Artic.* **1995**, *198*, 499–510. [[CrossRef](#)]
105. McOrist, G.D.; Smallwood, A. Trace Elements in Precious and Common Opals Using Neutron Activation Analysis. *J. Radioanal. Nucl. Chem.* **1997**, *223*, 9–15. [[CrossRef](#)]
106. Carter, J.; Riu, L.; Poulet, F.; Bibring, J.-P.; Langevin, Y.; Gondet, B. A Mars Orbital Catalog of Aqueous Alteration Signatures (MOCAAS). *Icarus* **2023**, *389*, 115164. [[CrossRef](#)]
107. Sun, V.Z.; Milliken, R.E. Distinct Geologic Settings of Opal-A and More Crystalline Hydrated Silica on Mars. *Geophys. Res. Lett.* **2018**, *45*, 10221–10228. [[CrossRef](#)]
108. Pan, L.; Carter, J.; Quantin-Nataf, C.; Pineau, M.; Chauviré, B.; Mangold, N.; Le Deit, L.; Rondeau, B.; Chevrier, V. Voluminous Silica Precipitated from Martian Waters during Late-Stage Aqueous Alteration. *Planet. Sci. J.* **2021**, *2*, 65. [[CrossRef](#)]
109. Gabriel, T.S.J.; Hardgrove, C.; Achilles, C.N.; Rampe, E.B.; Rapin, W.; Nowicki, S.; Czarnecki, S.; Thompson, L.; Nikiforov, S.; Litvak, M.; et al. On an Extensive Late Hydrologic Event in Gale Crater as Indicated by Water-Rich Fracture Halos. *J. Geophys. Res. Planets* **2022**, *127*, e2020JE006600. [[CrossRef](#)]

Disclaimer/Publisher’s Note: The statements, opinions and data contained in all publications are solely those of the individual author(s) and contributor(s) and not of MDPI and/or the editor(s). MDPI and/or the editor(s) disclaim responsibility for any injury to people or property resulting from any ideas, methods, instructions or products referred to in the content.